MSE | MASTER OF SCIENCE IN ENGINEERING

Predictive Maintenance Using Machine Learning for Printheads

Projet d'approfondissement (PA) — HEIA-FR

Title	Predictive maintenance using machine learning for printheads
Supervisor	Wolf Beat
Institution	HEIA-FR
Company	iPrint
Company representative	Fernando Rodriguez Llorente
GitHub repository	github.com/PA-iPrint-anomaly-detection/PA

Author: Anthony Atallah

January 8, 2026

Abstract

Inkjet printing has evolved from a graphics technology into a versatile manufacturing platform, enabling printed electronics, functional coatings and biofabrication. Ensuring the reliability of industrial printheads is therefore critical. In this report we develop and evaluate a machine-learning pipeline for predictive maintenance of piezoelectric drop-on-demand printheads. Starting from synchronised nozzle-check images and acoustic self-sensing signals recorded during controlled pressure sweeps, we extract a compact parametric representation of the nozzle ring-down, train supervised models to classify nozzle state (jetting versus missing line) and predict whether a nozzle will become non-jetting before the end of the sweep, and explore the extent to which pressure can be regressed from the acoustic features. Throughout, we highlight limitations arising from pressure-induced defect simulation and discuss the use of a complementary increasing-pressure dataset to assess robustness. The work serves as a foundation for deploying predictive maintenance in real production settings.

Contents

Chapter 1

Introduction

1.1 Background and motivation

Inkjet printing has evolved into a versatile manufacturing platform for printed electronics, functional coatings and biomedical patterning. At the heart of every system lies a printhead containing dense arrays of microscopic nozzles. Each nozzle ejects droplets at high frequency with tight tolerances on volume, position and timing; any degradation directly impacts print quality and process reliability. Common failure modes include clogging, partial wetting, satellite formation, misdirected jets and gradual reductions in ejected volume. These defects manifest as missing or faint lines, banding and graininess on the printed substrate. In industrial settings the prevailing maintenance practice relies on periodic visual inspections and simple nozzle-test patterns. Such inspections are labour-intensive, subjective and reactive: nozzles are serviced only after print quality has visibly degraded.

Predictive maintenance seeks to replace this reactive strategy with a data-driven, proactive approach: continuously monitor the condition of each nozzle, detect early signatures of degradation and intervene before failures become visible. In this work we make use of two complementary data modalities. First, printed nozzle-check images provide a direct visual record of whether each nozzle is jetting correctly. Second, acoustic self-sensing waveforms captured from the piezoelectric drive circuits contain rich dynamic information about the fluid–structure response during droplet ejection. Figure 1.1 shows an illustrative nozzle-check pattern; clean vertical lines correspond to healthy nozzles, whereas missing or distorted lines indicate defects. Integrating these modalities enables us to infer nozzle state and anticipate future failures without relying on manual inspection.

(a) Inkjet printhead with a dense array of microscopic nozzles (chip), where nozzle health directly affects print quality.

(b) Illustrative nozzle-check patterns: clean vertical lines indicate healthy nozzles, while missing or distorted lines reveal defective nozzles.
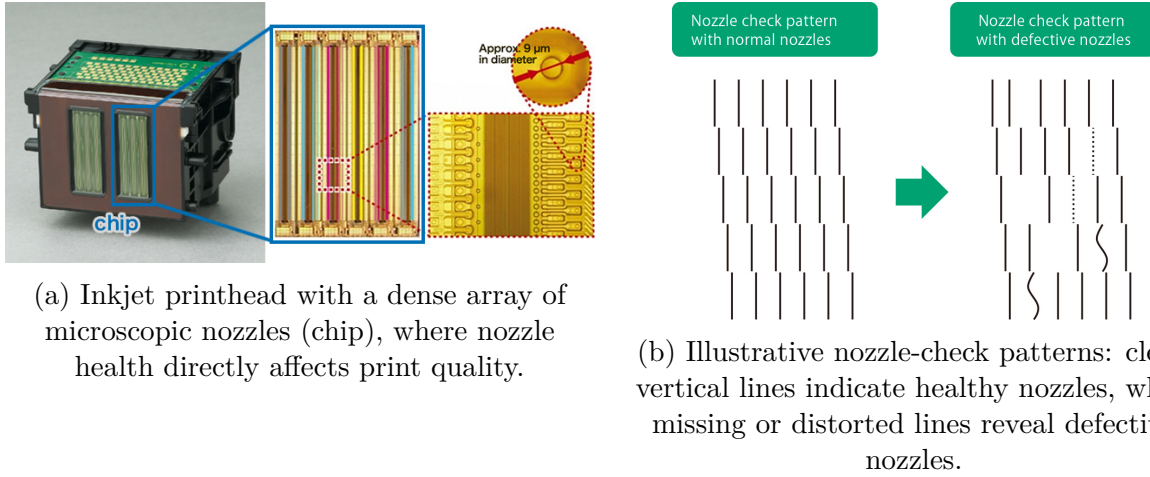
Figure 1.1: Nozzle-check images used for visual inspection and as ground-truth labels of nozzle state (healthy vs. defective) in our predictive-maintenance setting.

1.2 Project context and collaboration

This project was conducted at HEIA-FR in collaboration with the *iPrint* group in Fribourg. The iPrint institute provided the dataset of synchronised self-sensing waveforms and nozzle-check images used throughout this work, while the ISIS team supplied the image-based nozzle-state labels. The work was supervised at HEIA-FR by **M. Wolf Beat**, who provided scientific guidance throughout the project, helped refine the problem formulation and experimental protocol, and ensured methodological rigor in the modelling and evaluation choices.

In particular, **M. Fernando Rodriguez Llorente** from iPrint accompanied the project, clarified the operation of the self-sensing circuitry and the pressure-sweep protocol, and supported the interpretation of the parametric fits and the physical intuition underpinning the damped-sinusoid ring-down model. Overall, this collaboration ensured that the machine-learning developments presented here remain grounded in printhead physics and aligned with practical maintenance constraints.

1.3 Project scope and objectives

This report is prepared in the context of a *Projet d'approfondissement* at HEIA-FR under the supervision of Wolf Beat. The overarching question we address is:

> *How can acoustic self-sensing be exploited to automatically detect and anticipate printhead nozzle defects for predictive maintenance?*

Our scope and objectives are as follows:

- **Compact feature extraction.** Convert raw self-sensing waveforms into a compact, physically interpretable representation by isolating the ring-down and fitting a damped-sinusoid model. This representation should summarise the key dynamical characteristics of each nozzle while being robust to noise and baseline drift.

- **Nozzle-state inference.** Use supervised learning to classify each nozzle as *jetting* (printing an acceptable line) or *non-jetting* (missing line) based solely on acoustic features. To obtain ground truth we rely on labels generated automatically from nozzle-check images by an existing segmentation and classification algorithm provided by the ISIS/iPrint team (details in Chapter 3).

- **Predictive-maintenance forecasting.** Move beyond snapshot classification to predict whether a currently jetting nozzle will become non-jetting at any later step within the same pressure sweep. This anticipatory task corresponds to deciding whether maintenance should be scheduled before a defect appears on the substrate.

- **Dataset diagnosis.** Perform an exploratory regression of the meniscus pressure from the acoustic features. The aim is to quantify how strongly the features encode the controlled pressure trajectory; strong dependence indicates that pressure may confound defect inference and motivates cautious interpretation of results.

1.4   Report organisation

This introduction provides the motivation, scope and overview of the problem. Chapter 2 (State of the Art) then reviews the key background needed for the remainder of the report, covering piezoelectric printheads and acoustic self-sensing, as well as the machine-learning models and evaluation metrics used in this work. To streamline the narrative and avoid redundancy, detailed descriptions of the data acquisition and labelling process are deferred to Chapter 3. In that chapter we describe the printhead setup, the acquisition protocol, the label definitions produced by the ISIS algorithm and our rationale for excluding ambiguous categories. Chapter 4 presents the processing pipeline: ring-down extraction, parametric modelling via a damped-sinusoid, bank correction, and the formulation of classification and predictive-maintenance tasks. Chapter 5 summarises preliminary results and discusses limitations arising from pressure-induced defect simulation. Chapter 6 concludes the report with a synthesis of contributions and future directions.

Chapter 2

State of the Art

2.1 Piezoelectric printheads and acoustic self-sensing

Piezoelectric drop-on-demand printheads consist of arrays of microfabricated ink channels, each terminated by a tiny nozzle. A voltage pulse applied to a piezoelectric wall deforms the ink chamber, generating a pressure wave that ejects a droplet through the nozzle orifice. After the drive pulse, the coupled fluid–structure system relaxes and exhibits a damped oscillation. Through the direct piezoelectric effect, this oscillation induces a small voltage in the same electrodes used for actuation. The resulting *self-sensing* waveform therefore encodes the mechanical response of the nozzle cavity. Figure 2.1 sketches a simplified cross-section of a piezoelectric channel, highlighting the ink chamber, piezoelectric wall and nozzle. Because each nozzle has its own piezoelectric element and the electrical circuit can be instrumented during printing, acoustic self-sensing provides a non-invasive way to monitor nozzle dynamics at very high throughput.

(a) Principle of piezoelectric drop-on-demand actuation: a voltage pulse deforms the piezoelectric wall, generates a pressure wave in the ink chamber, and ejects a droplet through the nozzle.

(b) Acoustic self-sensing concept: after the drive pulse, the coupled fluid–structure system exhibits a damped oscillation that induces a measurable voltage on the same electrodes (direct piezoelectric effect).
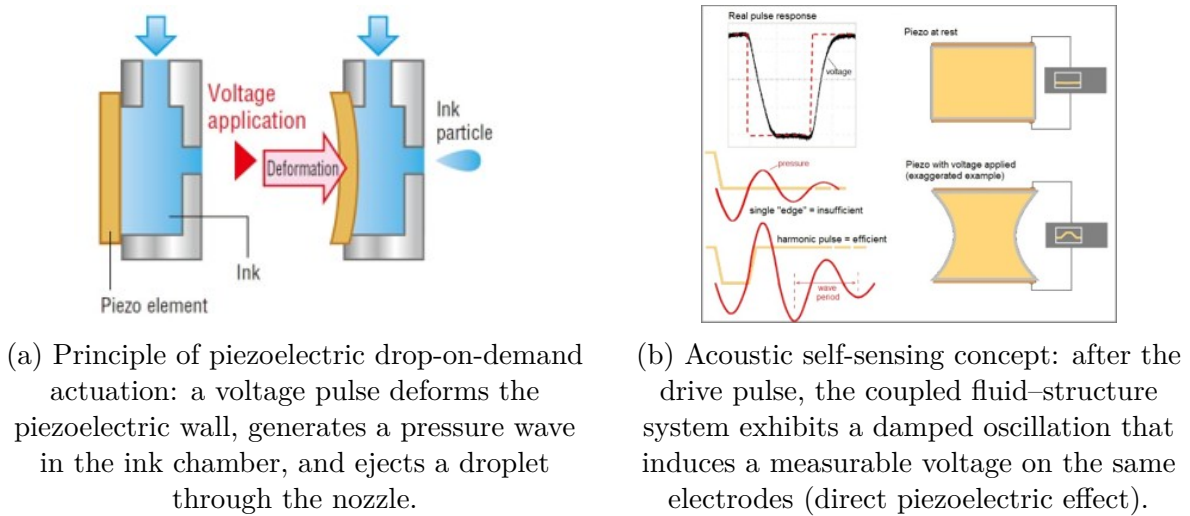
Figure 2.1: Piezoelectric actuation and self-sensing in drop-on-demand printheads.

As illustrated in Figure 4.5, the raw piezoelectric self-sensing waveform can be decom-

posed into three phases: (i) an initial capacitive lobe dominated by the drive electronics, (ii) a short settling transient of the measurement circuit, and (iii) the acoustic ring-down of the ink cavity (residual pressure oscillation). In this work, only the ring-down segment is retained for predictive maintenance. Section 4.1 explains how this segment is isolated, and Section 4.2 presents a compact parametric model to summarise it.
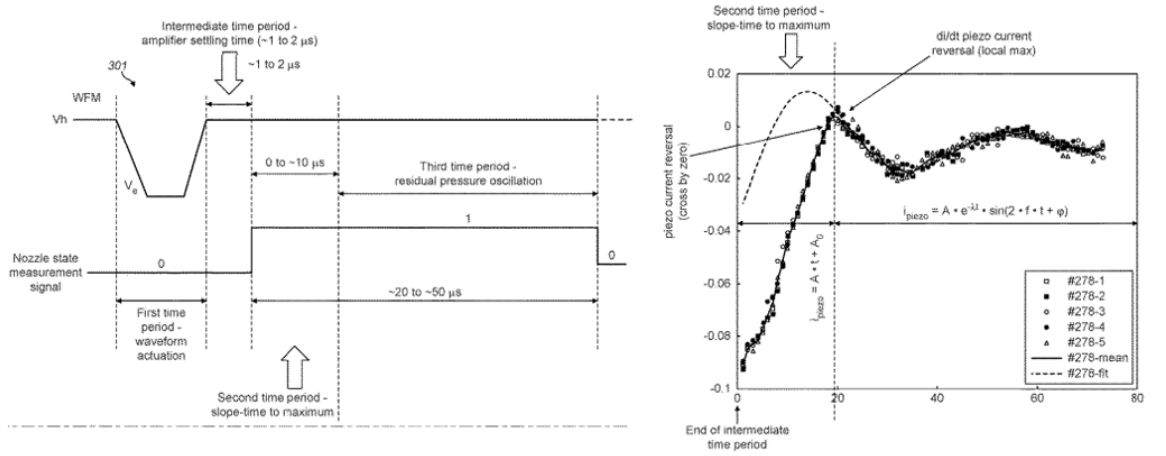

Figure 2.2: Raw self-sensing waveform and segmentation into the three phases considered in this work: capacitive actuation lobe, circuit settling transient, and acoustic ring-down (residual pressure oscillation).

2.2 Meniscus pressure and jetting stability

At the nozzle exit, the ink forms a curved free surface called the *meniscus*. The *meniscus pressure* denotes the pressure difference between the ink delivery system and the surrounding atmosphere at the nozzle opening. In industrial inkjet systems this pressure is typically maintained slightly negative (i.e., a small vacuum) so that ink is held inside the nozzle between firings and does not drip or wet the nozzle plate.

Meniscus pressure strongly influences jetting reliability and defect formation. If the bias is *too low in magnitude* (insufficient vacuum, closer to zero), ink can accumulate on the nozzle plate (flooding), which destabilises droplet formation and can lead to smearing or nozzle-to-nozzle interference. Conversely, if the bias is *too high in magnitude* (excessive vacuum, more negative), the nozzle can become ink-starved and may ingest air, leading to weak ejection or complete misfires (missing lines). Because the stable operating window can be narrow, controlled sweeps of meniscus pressure provide a practical way to reproduce jetting failures and study their signatures in self-sensing signals.
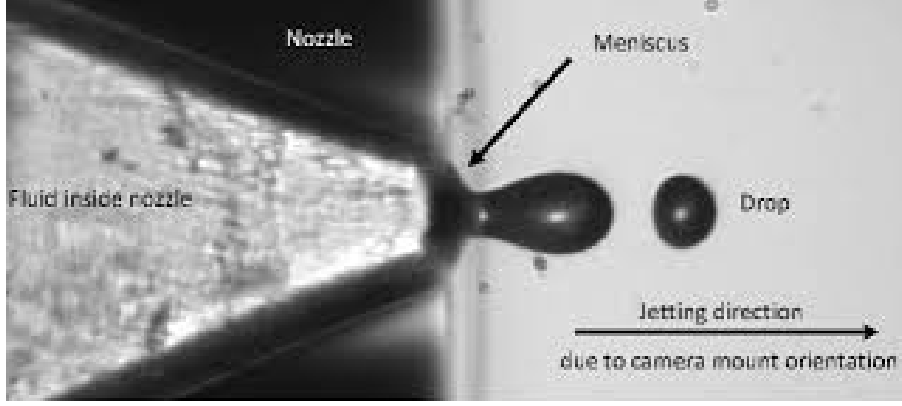
7

Figure 2.3: Annotated view of droplet ejection at the nozzle exit. The meniscus (free surface at the nozzle opening) is governed by the meniscus/bias pressure, which critically affects drop formation and the onset of defects such as wet-out (too little vacuum) or starvation/misfires (too much vacuum).

2.3 Machine learning models and evaluation metrics

The work presented in this report involves two main supervised learning tasks in this work: classification (detecting missing lines) and event prediction (anticipating future failures/predictive maintenance). Both tasks operate on the six-dimensional feature vectors $\bar{\theta} = (A, \tau, f, \phi, C, D)$ derived from the damped-sinusoid model.

2.3.1 Histogram-based gradient boosting classifiers

For both classification and predictive-maintenance experiments we employ *histogram-based gradient boosting classifiers* (HGB). Gradient boosting builds an ensemble of shallow decision trees where each tree corrects the residual errors of the previous ones. The histogram variant bins continuous features into discrete intervals to accelerate tree construction, making it well suited for medium-sized datasets. We choose HGB because it captures non-linear interactions between fitted parameters (for instance, joint variations of amplitude and decay) and is robust to heterogeneous feature scales. Hyperparameters (number of trees, maximum depth, learning rate) are tuned via cross-validation.
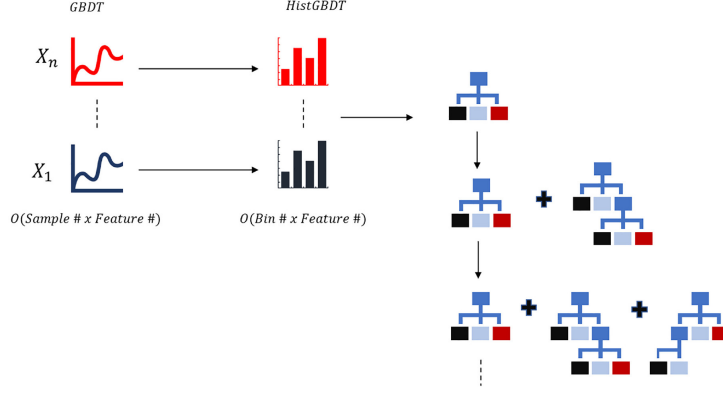
Figure 2.4: Schematic of histogram-based gradient boosting (HGB): continuous feature vectors are first discretised into bins (histograms), then an ensemble of shallow decision trees is built sequentially, each tree correcting the residual errors of the previous ones. The final prediction is obtained by aggregating the trees' outputs, enabling efficient modelling of non-linear interactions between features.

2.3.2 Evaluation metrics

We report model performance using the following metrics:

- **Accuracy**: the proportion of correctly classified instances. If TP denotes true positives, TN true negatives, FP false positives and FN false negatives, then

$$\text{Accuracy} = \frac{TP + TN}{TP + TN + FP + FN}.$$

- **Precision**: the fraction of predicted positives that are correct, Precision $= TP/(TP + FP)$. In the context of missing-line detection we typically treat the positive class as *non-jetting* (missing line), so precision quantifies how often a predicted defect is truly a defect.

- **Recall**: the fraction of actual positives that are detected, Recall $= TP/(TP + FN)$. For missing-line detection this measures the proportion of defects that are successfully flagged.

- **F1 score**: the harmonic mean of precision and recall, defined as

$$\text{F1} = 2\frac{\text{Precision} \cdot \text{Recall}}{\text{Precision} + \text{Recall}}.$$

This metric balances the trade-off between false alarms and missed detections.

Figure 2.5: Binary confusion matrix used to define the evaluation metrics. Rows correspond to predicted labels and columns to ground-truth labels, yielding true positives (TP), false positives (FP), false negatives (FN), and true negatives (TN) for the chosen positive class (here, typically *non-jetting*).

Chapter 3

Datasets and Labels

3.1 Data acquisition and sampling

The primary dataset used in this report consists of synchronised acoustic self-sensing waveforms and printed nozzle-check images acquired from a single piezoelectric drop-on-demand printhead. The printhead comprises four electrical banks (A–D) driving 320 nozzles each, for a total of 1280 nozzles.

The experiments involve controlled pressure sweeps to simulate different operating conditions and induce missing-line defects. In this report, the reported pressure corresponds to the *nozzle meniscus pressure*, i.e., the pressure difference between the ink delivery system and the atmosphere (see Section 2.2).

Across both sweep families, two replicates are available. Replicate 1 is recorded after printing a standard nozzle-check image that is *not* a solid-black print, whereas replicate 2 is recorded after printing a solid-black test image. This second condition was included to help reveal potential ink-related effects; however, investigating ink-related phenomena is beyond the scope of this work.

The two available families of sweeps:

Lowering pressure sweep (main dataset). The pressure decreases from -50 mbar to -87.6 mbar in 0.4 mbar increments, resulting in 95 distinct pressure levels. This dataset provides our primary training and evaluation platform.

Increasing pressure sweep (robustness dataset). To assess the generalisation of learned models, we use a complementary sweep in which pressure increases from -50.0 mbar to -44.0 mbar, again in 0.4 mbar steps. This sequence covers a narrower, more stable operating range and serves to test whether observations made on the lowering sweep carry over to a different pressure trajectory.

For each pressure step and replicate we collect:

- A `Sensing.json` file containing the raw self-sensing waveforms for all banks. Each waveform is sampled at 4.125 MHz and consists of 124 samples in the captured window. As described in Section 4.1, we discard the first 35 samples dominated by the direct actuation response and use the remaining 89 samples as the ring-down segment.

- A corresponding bitmap image of the printed nozzle-check pattern. From the filename we extract the meniscus pressure. The images are processed by the ISIS segmentation algorithm to generate nozzle-state labels.
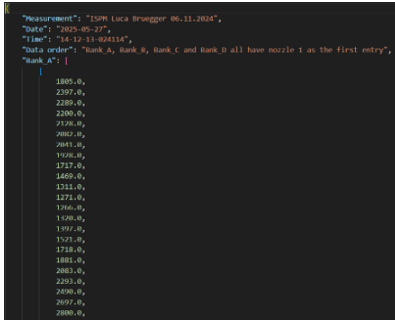
(a) Example of a `Sensing.json` acquisition snapshot at one pressure step, showing how the raw self-sensing waveforms are stored for all banks/nozzles (sampled at 4.125 MHz, 124 samples per waveform).
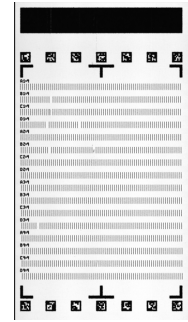
(b) Example nozzle-check bitmap acquired at the same pressure step and used for label generation: the printed test pattern is processed by the ISIS segmentation pipeline to assign nozzle-state labels.

Figure 3.1: Two synchronised data modalities collected at each pressure step: raw acoustic self-sensing waveforms (`Sensing.json`) and the corresponding printed nozzle-check image used to derive nozzle-state labels.

3.2 Label generation using the ISIS algorithm

Nozzle-state labels are obtained from the printed nozzle-check images using a labelling algorithm provided by the ISIS/iPrint team. This procedure is external to the present work. We use its outputs as supplied and do not modify, re-train, or re-derive the labels.

At each pressure step, the algorithm returns one categorical label per nozzle (1280 labels per image). The classes emitted by the algorithm are:

- **Jetting:** an acceptable, continuous printed line.

- **Non-jetting:** no discernible printed line (missing line).

- **Intermittent:** the line is not printed continuously (broken/dashed segments), indicating inconsistent jetting.

- **Deviated:** a printed line that is present but laterally displaced from its nominal position.
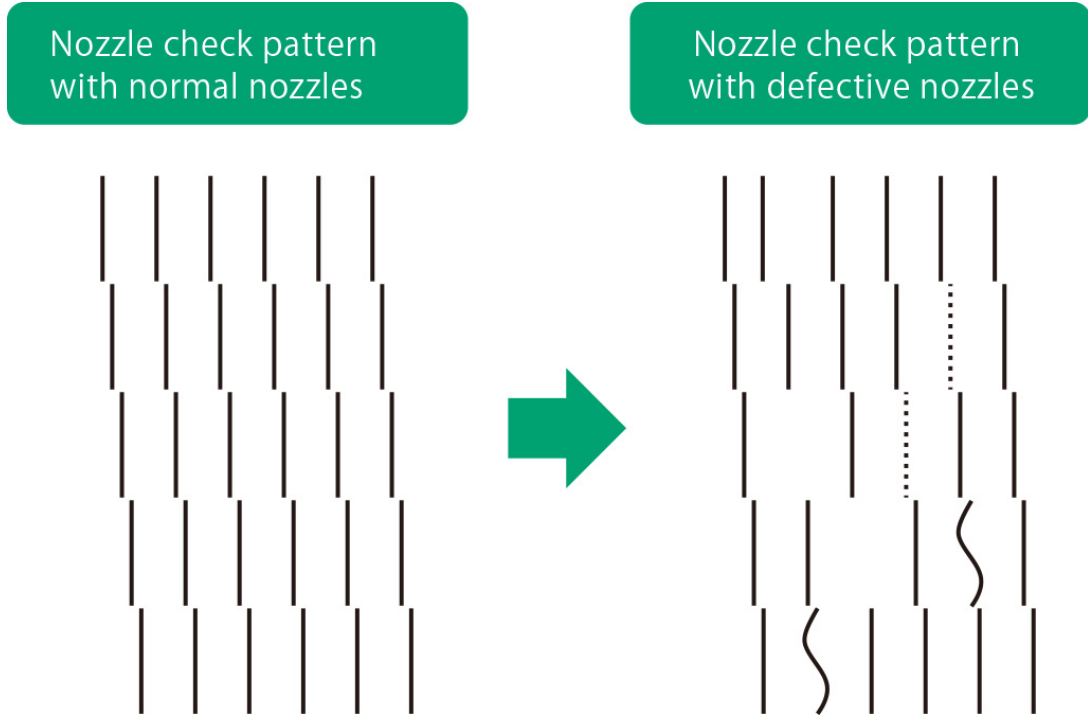
Figure 3.2: Illustration of nozzle-check patterns. Left: normal (jetting) nozzles produce continuous printed lines. Right: defective nozzles yield characteristic artefacts such as missing lines (non-jetting), broken/dashed lines (intermittent), or displaced lines (deviated).

In the remainder of this work, these image-derived labels are treated as the reference nozzle states for training and evaluating models based on acoustic self-sensing signals.

Table 3.1 reports the number of samples per label for each dataset returned by the ISIS/iPrint labelling pipeline. In addition to the four primary nozzle states used throughout this work, the algorithm occasionally emits *Other* category.

Dataset	Jetting	Non-jetting	Intermittent	Deviated	Other
Lowering rep. 1	117 375	2 938	507	777	3
Lowering rep. 2	116 837	3 139	447	1 173	4
Increasing rep. 1	12 506	1 173	13	353	35

Table 3.1: Number of nozzle×pressure samples per label produced by the ISIS/iPrint algorithm for each dataset.

3.3   Excluded classes and rationale

Upon inspecting the raw labels we noticed that the *intermittent* and *deviated* categories behave erratically: a nozzle may be tagged as intermittent or deviated at one pressure step and then return to *jetting* at the next. Figure 3.3 illustrates this behaviour on two

consecutive pressure steps, where the locations of intermittent/deviated marks appear and disappear right after.

To verify whether these transient label changes correspond to a meaningful acoustic change, we compared fitted ring-down parameters across episodes of the form *jetting →* (*intermittent* or *deviated*) → *jetting*. In practice, the parameter values observed during *jetting* remain essentially unchanged. As a representative example, Figure 3.3c reports the episode-wise change in ring-down frequency Δf: the nominal frequency is on the order of $150\,\mathrm{kHz}$, while the distribution of Δf is centred near zero (median ≈ 0) with a spread of roughly $1.5\,\mathrm{kHz}$ (about 1% of the nominal value). The same qualitative behaviour is observed for the other fitted parameters.

As a result, these classes offer limited value for predictive maintenance because an event that vanishes one step later is not actionable. To keep the learning problem focused and to avoid training on noisy labels, we therefore restrict the supervised tasks to the following two labels:

**Jetting.** The printed line is present and deemed acceptable.

Non-jetting. The printed line is entirely absent (missing line).

Samples labelled as intermittent or deviated are retained only for descriptive analysis and visual inspection. They are omitted from all supervised training and evaluation to ensure that the classification and predictive-maintenance tasks are well defined and driven by meaningful, persistent signal differences.

(a) Nozzle-label map at one pressure step (example: $-52.0\,\text{mbar}$).

(b) Consecutive step (example: $-52.4\,\text{mbar}$) showing that intermittent/deviated tags appear/disappear across steps.
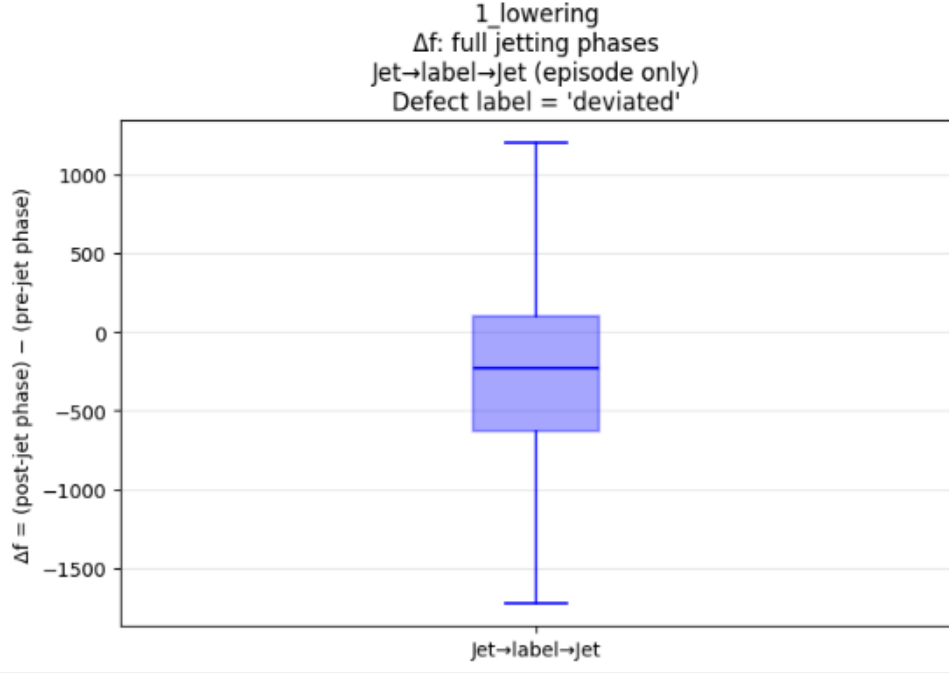
(c) Episode-wise change in ring-down frequency for *jetting→deviated→jetting*: the distribution is centred near zero (median ≈ 0) with a spread of $\approx 1.5\,\text{kHz}$, i.e., about 1% of a nominal $150\,\text{kHz}$ frequency. Similar patterns are observed for the other fitted parameters.

Figure 3.3: Intermittent/deviated labels are transient (flicker across consecutive pressure steps) and do not correspond to a persistent change in the fitted ring-down parameters, motivating their exclusion from supervised learning.

Chapter 4

Methods

4.1   Preprocessing and ring-down extraction

Each self-sensing waveform contains the response of the piezoelectric actuator and the coupled fluid–structure system to a drive pulse. The 124 captured samples can be divided into three phases: (1) a capacitive lobe dominated by the drive electronics, (2) a short transition while the analogue amplifiers settle, and (3) the acoustic ring-down of the nozzle cavity. Only the last phase carries information about nozzle health.

Empirically, the first 35 samples are dominated by the capacitive and settling phases. We therefore perform a fixed crop, discarding these samples and retaining the remaining 89 samples as the ring-down segment. We organise the cropped data into a three-dimensional tensor $\tilde{\mathbf{X}} \in \mathbb{R}^{1280 \times 95 \times 89}$, where the axes correspond respectively to nozzles, pressure levels and time samples. Figure 4.1 shows several raw waveforms and the extracted ring-down segment.

(a) Raw self-sensing waveforms (example nozzle across multiple pressures).
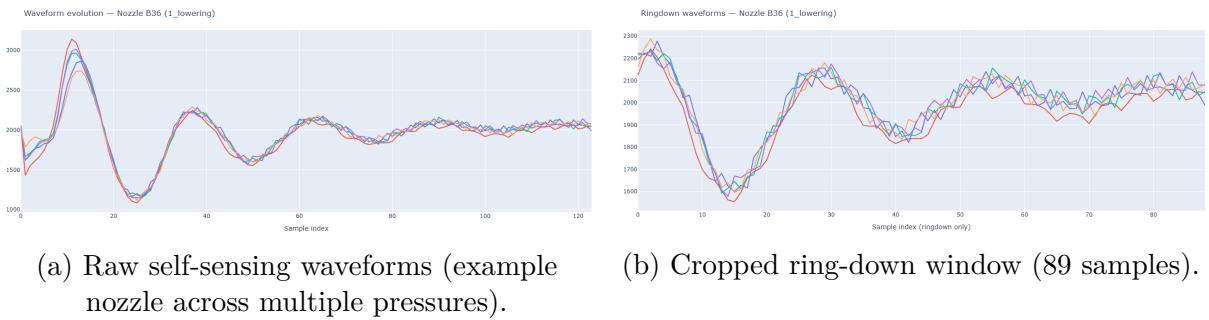
(b) Cropped ring-down window (89 samples).

Figure 4.1: Ring-down extraction from raw self-sensing waveforms: a fixed crop removes the direct actuation and settling phases, leaving the acoustic ring-down used for subsequent modelling.

4.2 Parametric modelling of the ring-down

Each 89-sample ring-down segment encodes the oscillatory response of the nozzle cavity. To summarise this response we fit a damped sinusoid with a linear baseline:

$$y(t) = C + Dt + A\exp\left(-\frac{t}{\tau}\right)\sin\left(2\pi f t + \phi\right), \tag{4.1}$$

where A sets the oscillation amplitude, τ controls the decay rate, f denotes the dominant frequency, ϕ is the phase offset, and the linear term $(C + Dt)$ captures static offset and slow drift. Figure 4.2 illustrates how these terms shape the signal and shows a typical fit on a measured ring-down trace.
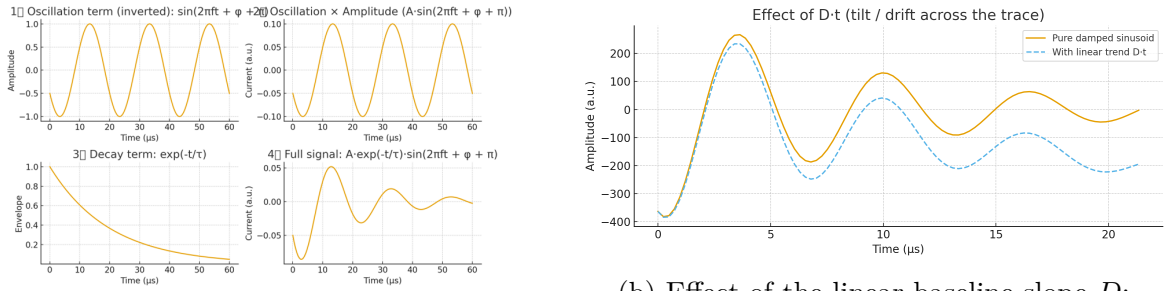
(a) Contribution of the sinusoidal term and exponential envelope: A scales the oscillation, τ controls the decay, f sets the period, and ϕ shifts the waveform in time (phase convention).

(b) Effect of the linear baseline slope D: adding the Dt term models slow drift/tilt across the window and prevents (A, τ, ϕ) from compensating for baseline variations.
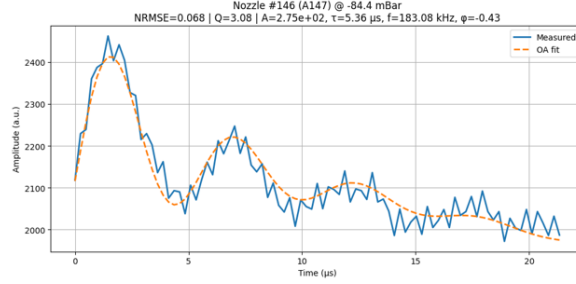
(c) Example of a fitted model (orange) over a measured ring-down segment (blue), illustrating that the parameters compactly capture the dominant oscillatory behaviour.

Figure 4.2: Interpretation of the damped-sinusoid model in Eq. (4.1): oscillatory component (A, τ, f, ϕ) and baseline terms (C, D), illustrated on synthetic contributions and a representative fit on measured data.

4.2.1 Model interpretation

The six parameters in Equation (4.1) have intuitive meanings:

- **Amplitude** A: magnitude of the oscillation. Larger values indicate stronger ringing and greater energy stored in the fluid–structure system.

- **Decay time** τ: rate at which the oscillation dies out. A larger τ corresponds to a slowly decaying ring-down.

- **Frequency** f: principal oscillation frequency, reflecting the natural resonance of the ink cavity and piezoelectric structure.

- **Phase** ϕ: horizontal shift relative to the start of the ring-down; sensitive to the polarity convention of the sensing circuit.

- **Baseline offset** C and **slope** D: account for static offset and slow drift across the window. Including these terms prevents biasing (A, τ, ϕ) to compensate for baseline variations.

4.2.2 Fitting procedure

Because direct global optimisation of Equation (4.1) is prone to local minima and sensitive to noise, we employ a two-step approach combining robust initialisation with windowed fitting and overlap–add reconstruction. The main steps are summarised below.

Initial parameter estimates. For each waveform (or each sliding window, described below) we compute rough initial values:

- *Baseline C_0 and D_0*: estimate the linear baseline $C_0 + D_0 t$ by least squares and remove it from the waveform to isolate the oscillatory component (detrending).

- *Dominant frequency f_0*: estimate from the peak of the tapered FFT magnitude, refined by parabolic interpolation.
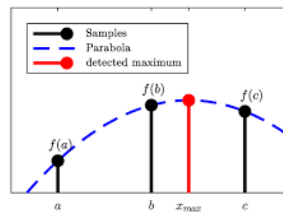
- *Amplitude A_0*: obtain from the peak-to-peak range of the detrended signal.

- *Decay time τ_0*: detect peaks in the absolute detrended signal and fit a line to the logarithm of peak magnitudes versus time; the slope yields an estimate of the decay rate γ_0.

Detected Envelope Peaks on Signal
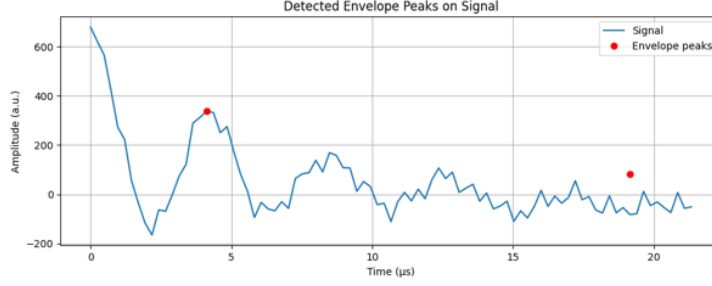
- *Phase ϕ_0*: estimate from the signal value and its initial slope, using a finite-difference approximation of $y'(t)$ and $\phi_0 \approx \mathrm{atan2}(2\pi f_0\, y(t_0),\, y'(t_0))$ (after detrending).

Windowed robust optimisation. Rather than fit the entire ring-down at once, we slide a window of length L (approx. six cycles at f_0) across the 89-sample segment with 50% overlap. In each window we perform robust non-linear least squares with a soft-ℓ_1 loss to mitigate the influence of outliers. Practical bounds are imposed on all parameters. To reduce sensitivity to local minima we employ a small multi-start search: we perturb (f, ϕ) around the initial estimates and retain the fit with the lowest normalised RMSE. To encourage temporal smoothness, we constrain each window's parameters to lie within multiplicative or additive bands relative to the previous window's solution, preventing abrupt jumps due to noise.

Overlap–add reconstruction and parameter averaging. Each window produces a local fit $\hat{y}_w(t)$ and parameter vector $\theta_w = (A_w, \tau_w, f_w, \phi_w, C_w, D_w)$ with an associated normalised error. We combine the local fits into a single smooth reconstruction via overlap–add synthesis:

$$\hat{y}_{\mathrm{OLA}}(t) = \frac{\sum_w w(t)\, \hat{y}_w(t)}{\sum_w w(t)},$$

where $w(t)$ is a function weighting each window. For downstream tasks we summarise the per-window parameters into a single feature vector by computing a weighted average, where weights are inversely proportional to the window errors. The phase is averaged using a circular mean to handle wrap-around at $\pm\pi$. The resulting feature vector:

$$\bar{\theta} = (\bar{A}, \bar{\tau}, \bar{f}, \bar{\phi}, \bar{C}, \bar{D})$$

serves as the acoustic representation of the ring-down. We also retain fit-quality metrics RMSE and NRMSE for diagnostic purposes.
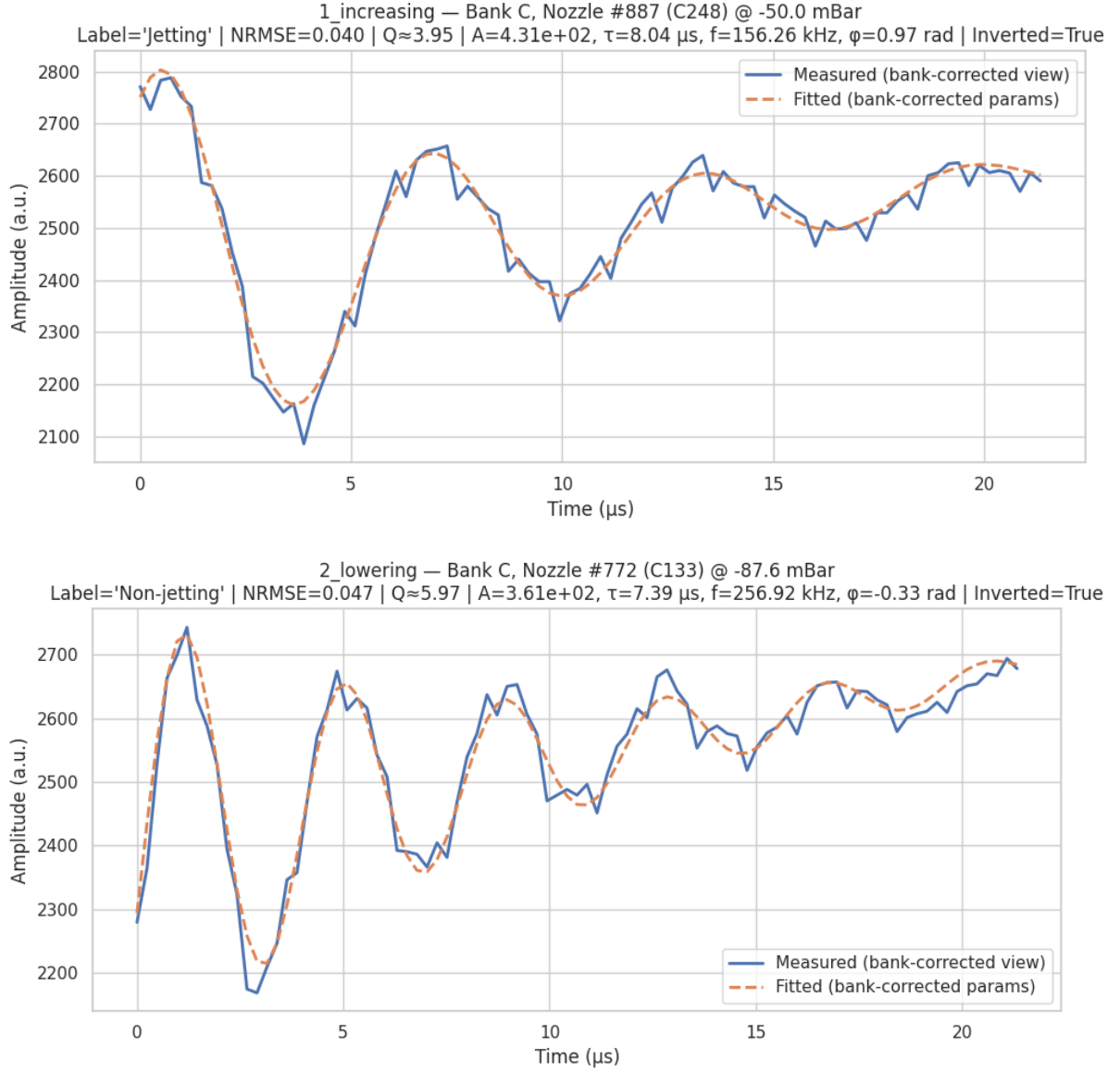
19

Figure 4.3: Representative ring-down fits produced by the windowed robust optimisation and overlap–add reconstruction. Top: jetting example (increasing rep. 1). Bottom: non-jetting example (lowering rep. 2). Solid lines show the measured (bank-corrected) signal; dashed lines show the fitted reconstruction evaluated using the averaged parameters $\bar{\theta} = (\bar{A}, \bar{\tau}, \bar{f}, \bar{\phi}, \bar{C}, \bar{D})$.
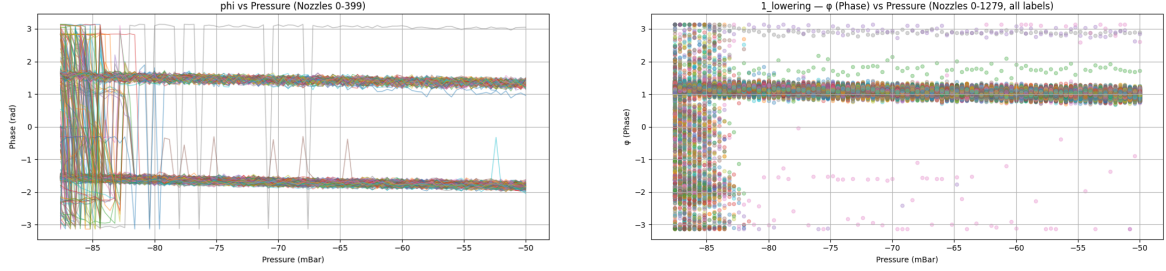
4.3 Phase and bank correction

The four printhead banks use different wiring and sensing paths, which can introduce an effective polarity inversion in the recorded self-sensing waveforms. In our dataset, banks A and C are inverted relative to banks B and D. When fitting our damped sinusoid model, this polarity flip appears primarily as a phase offset of approximately $\pi \pmod{2\pi}$. As a result, the fitted phase φ can become artificially bank-dependent, creating spurious structure in φ–pressure space (Fig. 4.4a) and potentially confounding downstream

20

classifiers.

To enforce a common phase convention, we apply a deterministic reflection *before* fitting: waveforms from banks A and C are reflected around their mid-value, while those from banks B and D are left unchanged. For a waveform $y(t)$ with minimum $y_{\min}$ and maximum $y_{\max}$, we define

$$y_{\mathrm{inv}}(t) = 2\, y_{\mathrm{mid}} - y(t), \qquad y_{\mathrm{mid}} = \frac{y_{\min} + y_{\max}}{2}.$$

This operation flips the oscillatory component without shifting the baseline and is equivalent (in the sinusoidal fit) to adding a constant π phase shift. After correction, φ is expressed in a consistent convention across all banks and varies smoothly with pressure (Fig. 4.4b), while the remaining parameters (e.g., A, τ, f) remain physically comparable. We store a boolean inversion mask alongside the data to document which waveforms were corrected.

(a) Before bank correction: bank-dependent polarity inversions manifest as an apparent π phase offset (and wrap-related discontinuities) in φ versus pressure.

(b) After bank correction: fitted φ traces are shown as continuous trajectories (subset of nozzles) and follow a shared phase convention across the pressure sweep.

Figure 4.4: Effect of printhead bank polarity on the fitted phase parameter φ. The deterministic reflection step removes bank-dependent sign inversions and yields a consistent phase convention across banks.

4.4 Nozzle-state classification

Each (nozzle, pressure) pair yields a six-dimensional acoustic feature vector $\bar{\theta}$ and a categorical label from the ISIS algorithm (Chapter 3). For classification we restrict the labels to two stable classes: *jetting* (acceptable line) and *non-jetting* (missing line), discarding intermittent and deviated categories (Section 3.3). We treat non-jetting as the positive class, since missing lines are the events of interest.

We split the data by nozzle to prevent leakage: all pressure steps from a given nozzle belong to the same partition. From the first replicate of the lowering sweep (`1_lowering`) we construct a training set by retaining all non-jetting examples and randomly subsampling an equal number of jetting examples to form a balanced dataset. A balanced held-

out test set is built similarly from the remaining nozzles in `1_lowering`. After training, the classifier is evaluated on four disjoint evaluation sets:

- **Balanced held-out test:** balanced subset of `1_lowering`, used to assess sensitivity and specificity under class balance.

- **Full dataset minus training signals:** all (nozzle, pressure) pairs from `1_lowering` excluding those used for training, preserving the natural class imbalance. This evaluation reflects realistic prevalence of missing lines.

- **Cross-replicate transfer:** full dataset from the second replicate of the lowering sweep (`2_lowering`). This evaluates whether a model trained on replicate 1 generalises to replicate 2 under the same pressure trajectory.

- **Cross-sequence transfer:** full dataset from the first replicate of the increasing sweep (`1_increasing`). This test probe the generalisation of the model to a different pressure trajectory.

We employ a histogram-based gradient boosting classifier (HGB) (see Chapter 2) trained on the six acoustic parameters. Hyperparameters (number of trees, maximum depth and learning rate) are tuned by cross-validation on the training set.

Performance is reported using accuracy, precision, recall and F1 score with respect to the positive class (non-jetting), as defined in Chapter 2. Because missing-line events are rare, we interpret the confusion matrix in terms of *missed defects* (FN) and *false alarms* (FP), i.e., jetting samples predicted as non-jetting.

4.4.1 Feature dependence analysis (distance correlation)

To characterise statistical dependencies among the fitted acoustic parameters and to assess how strongly each parameter relates to nozzle state, we compute a pairwise *distance correlation* matrix over the variables (A, τ, f, ϕ, C, D), the pressure and the binary label (jetting vs. non-jetting). Distance correlation is a non-parametric dependence measure that detects both linear and non-linear associations, taking values in $[0, 1]$ (0 indicates independence).The resulting matrix is reported in the Results section (Fig. 5.2) and is used only for descriptive analysis.

4.5 Predictive maintenance task

Beyond snapshot classification, we formulate a *predictive–maintenance* target: use the current acoustic signature to anticipate whether a nozzle will become non–jetting before

the end of the sweep. Let $z_t \in \{0, 1\}$ denote the nozzle state at sweep step t (1 for non–jetting and 0 for jetting). For each nozzle we define the onset index

$$t^\star = \min\{t : z_t = 1\},$$

with $t^\star = \infty$ if the nozzle never becomes non–jetting.

As illustrated in Fig. 4.5, we introduce a lead time $K \geq 1$ and define a sampling offset relative to the onset. For nozzles that fail ($t^\star < \infty$), we extract the acoustic feature vector K steps before onset (i.e., at $t = t^\star - K$) and assign a positive label ($y = 1$), corresponding to *eventual failure*. For nozzles that never fail ($t^\star = \infty$), we extract features from the latest available labelled step and assign a negative label ($y = 0$). When constructing balanced training sets, negative samples are drawn at step positions matched to the positive sampling offsets to avoid trivial time–in–sweep cues.

In contrast to snapshot classification, this dataset depends on the chosen lead time K through the *relative sampling position* (the offset $t^\star - K$ in Fig. 4.5), but the nozzle–level train/test split remains fixed. We therefore create a single split of nozzles and reuse it for all values of K. Differences observed across K are then attributable to the prediction horizon rather than changes in the data partition.

We train a histogram–based gradient boosting classifier on the six acoustic parameters using pooled training examples from multiple lead times ($K = 1, \ldots, 10$). At evaluation time, we report performance separately for each K by probing the same trained model with features extracted at the corresponding offset. Performance is summarised with accuracy, precision, recall, and F1 scores on held–out nozzles, and additionally on unseen replicates and sweep sequences.
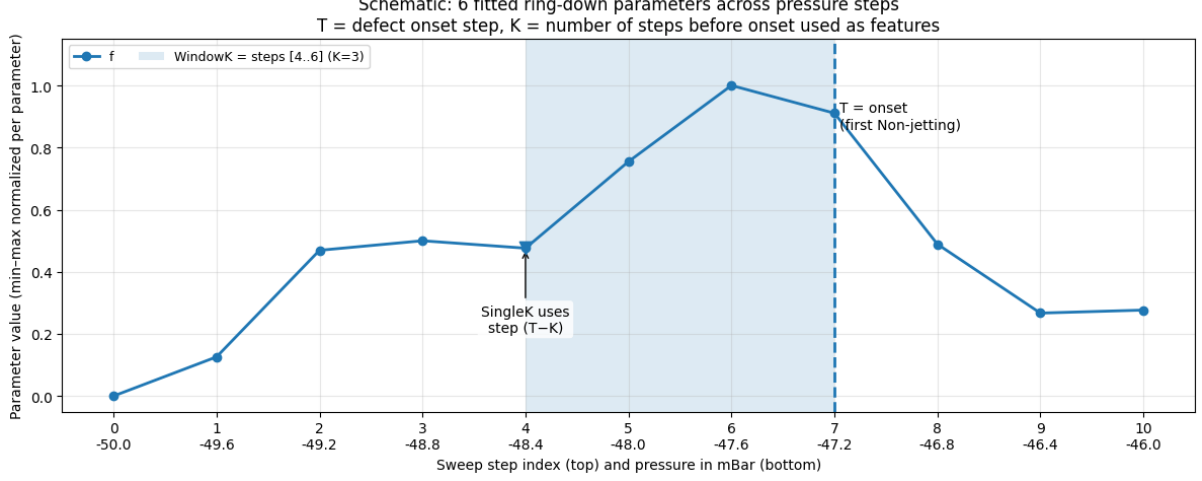
Figure 4.5: Schematic of the predictive–maintenance sampling rule across sweep steps. The dashed vertical line marks the defect onset step $t^\star$ (first non–jetting). For a chosen lead time K, the feature vector for failing nozzles is taken at $t = t^\star - K$ (i.e., K steps before onset) and labelled positive ($y = 1$); non–failing nozzles are sampled at their last labelled step and labelled negative ($y = 0$).

4.6 Exploratory pressure regression

Although pressure regression is not our primary objective, we use it as a diagnostic to quantify how strongly the fitted ring-down parameters are driven by pressure alone. Each summarised feature vector $\bar{\theta}$ (Section 4.2) is paired with the meniscus pressure p, and a non-linear regressor is trained to predict p from (A, τ, f, ϕ, C, D). We use histogram-based gradient boosting (with the same preprocessing as the classification pipeline: median imputation and robust scaling). The split is performed **by nozzle** to avoid leakage across pressure steps from the same nozzle. Performance is reported using R^2 and absolute/mean-square error metrics on held-out nozzles.

The results and regression diagnostic plot are presented in Section 5.3.

Chapter 5

Results and Discussion

5.1 Classification results

The histogram-based gradient boosting classifier trained on the six acoustic parameters achieves near-perfect separation of jetting and non-jetting samples on the lowering sweeps. Table 5.1 summarises performance on (i) a balanced held-out test from the first lowering replicate, (ii) the full first lowering replicate with training signals removed, (iii) the full second lowering replicate, and (iv) the full first increasing replicate. Figure 5.1 shows representative confusion matrices.

Evaluation set	n	#Jetting	#Missing	Acc.	Prec.	Rec.	F1
Lowering rep. 1 (balanced test)	1002	501	501	0.999	1.000	0.998	0.999
Lowering rep. 1 (full excl. train)	115 439	114 938	501	0.997	1.000	0.997	0.999
Lowering rep. 2 (full)	119 976	116 837	3 139	0.998	1.000	0.998	0.999
Increasing rep. 1 (full)	13 679	12 506	1 173	0.955	1.000	0.951	0.975

Table 5.1: Binary nozzle-state classification results using a histogram-based gradient boosting classifier on acoustic features (A, τ, f, ϕ, C, D). Precision, recall and F1 refer to the positive class (missing line).

On the balanced held-out test set, the classifier misclassifies only one jetting sample while correctly identifying all 501 missing-line samples (F1 $\approx$ 1 for the positive class). Across the full lowering sweeps, missed defects are essentially absent: 0 out of 501 missing-line samples in replicate 1 and 2 out of 3 139 in replicate 2 are misclassified. The remaining errors are predominantly false alarms, where jetting samples are flagged as non-jetting. Despite the different pressure trajectory and narrower range in the increasing sweep, performance remains strong with only one missed defect (accuracy 0.955, F1 0.975). Overall, these results indicate that the fitted ring-down parameters provide a robust acoustic signature of non-jetting events and that the learned decision rule transfers reliably across

replicates and pressure profiles.

(a) Lowering rep. 1 (balanced test)

(b) Lowering rep. 1 (full excl. train)

(c) Lowering rep. 2 (full)
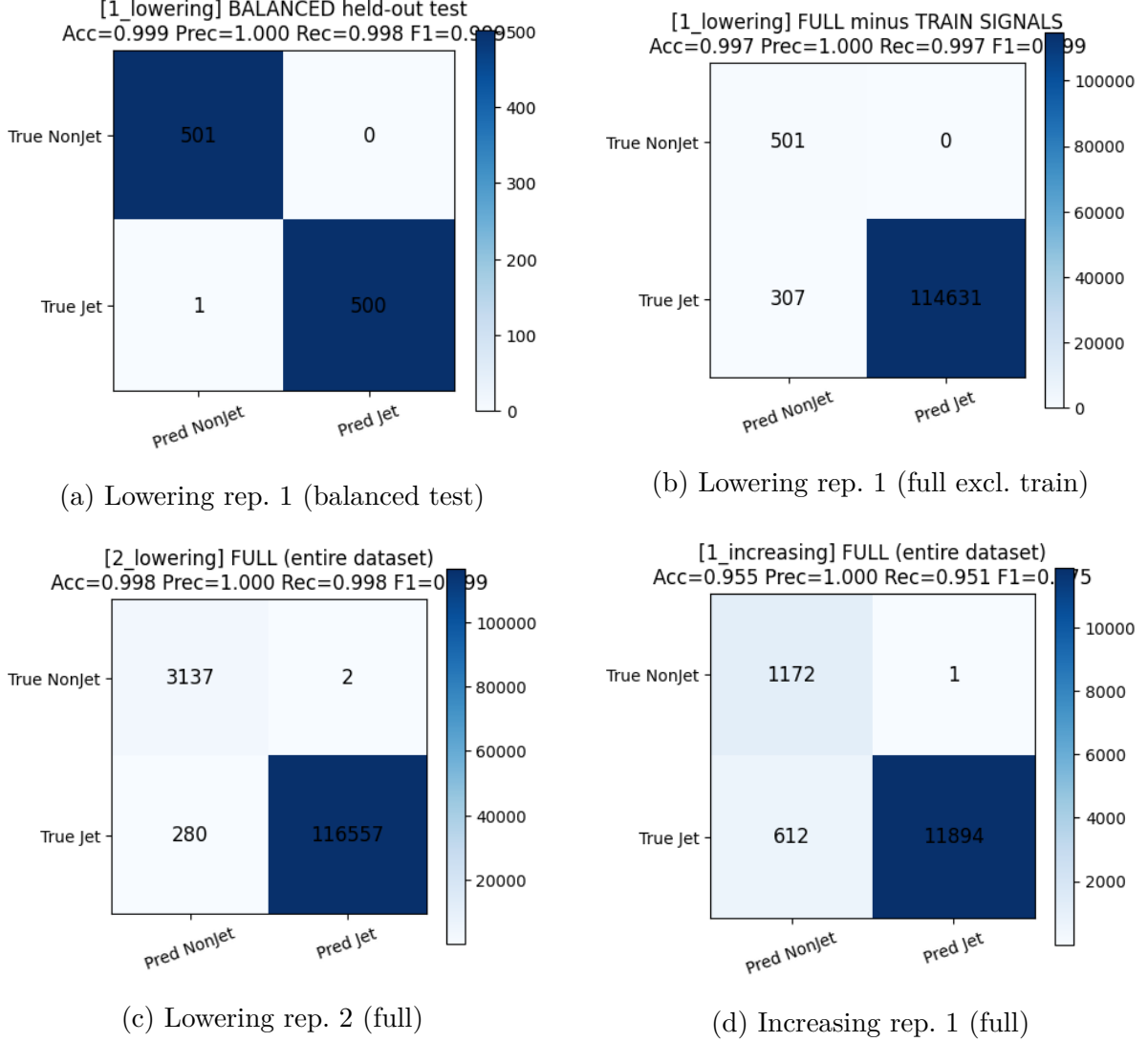
(d) Increasing rep. 1 (full)

Figure 5.1: Confusion matrices for the four evaluation sets reported in Table 5.1: (a) balanced held-out test from lowering rep. 1, (b) full lowering rep. 1 with training signals removed, (c) full lowering rep. 2, and (d) full increasing rep. 1. Values correspond to counts of (true label, predicted label) pairs.

5.1.1 Dependence structure via distance correlation

Although pressure is not used as an input to the classifier, we analyse the dependence structure between the fitted acoustic parameters, the meniscus pressure, and the nozzle-state label to assess dataset structure and potential confounding effects. Figure 5.2 shows the distance-correlation matrix for the first lowering sweep.

The label is most strongly associated with the oscillatory parameters, especially the fitted frequency f (distance correlation ≈ 0.86) and phase ϕ (≈ 0.60). In contrast, the marginal dependence between meniscus pressure and the label is moderate (≈ 0.22). This indicates that pressure alone is not a strong surrogate for nozzle state across the full

sweep: most observations remain jetting over a wide pressure range, while defects emerge predominantly in the low-pressure tail in a non-linear, threshold-like regime. Parameters C and D show near-zero dependence with the label, indicating limited discriminative value in this setting.
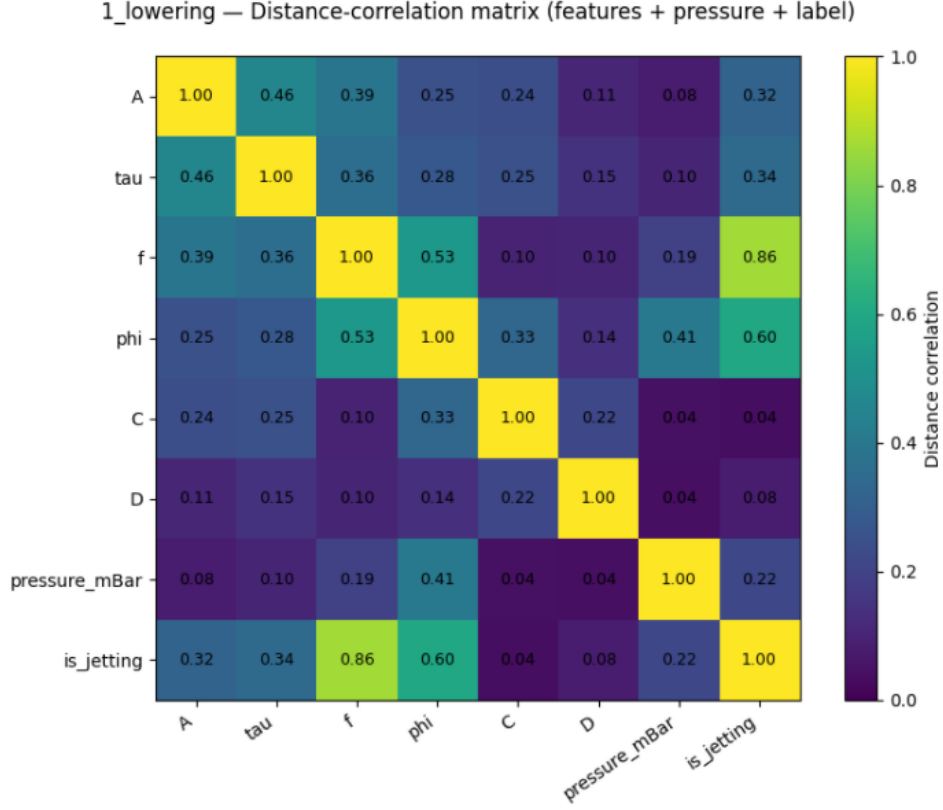

Figure 5.2: Distance-correlation matrix between the fitted acoustic parameters (A, τ, f, ϕ, C, D), the meniscus pressure, and the binary nozzle-state label (jetting vs. non-jetting), computed on a random subsample of 10000 observations.

The strong distance-correlation of the label with f and ϕ is consistent with their marked pressure dependence: both parameters display substantial non-linear drift and heteroscedasticity in the lowest-pressure regime, which coincides with the region where the vast majority of non-jetting samples are observed. Consequently, the marginal association between $\{f, \phi\}$ and `is_jetting` is expected to be amplified by the label's highly non-uniform support over pressure, whereas τ and A remain comparatively invariant across the sweep and therefore exhibit weaker dependence with the class indicator.

(a) Frequency f (mean $\pm$ 1 SD)

(b) Phase ϕ (mean $\pm$ 1 SD)

(c) Damping time τ (mean $\pm$ 1 SD)

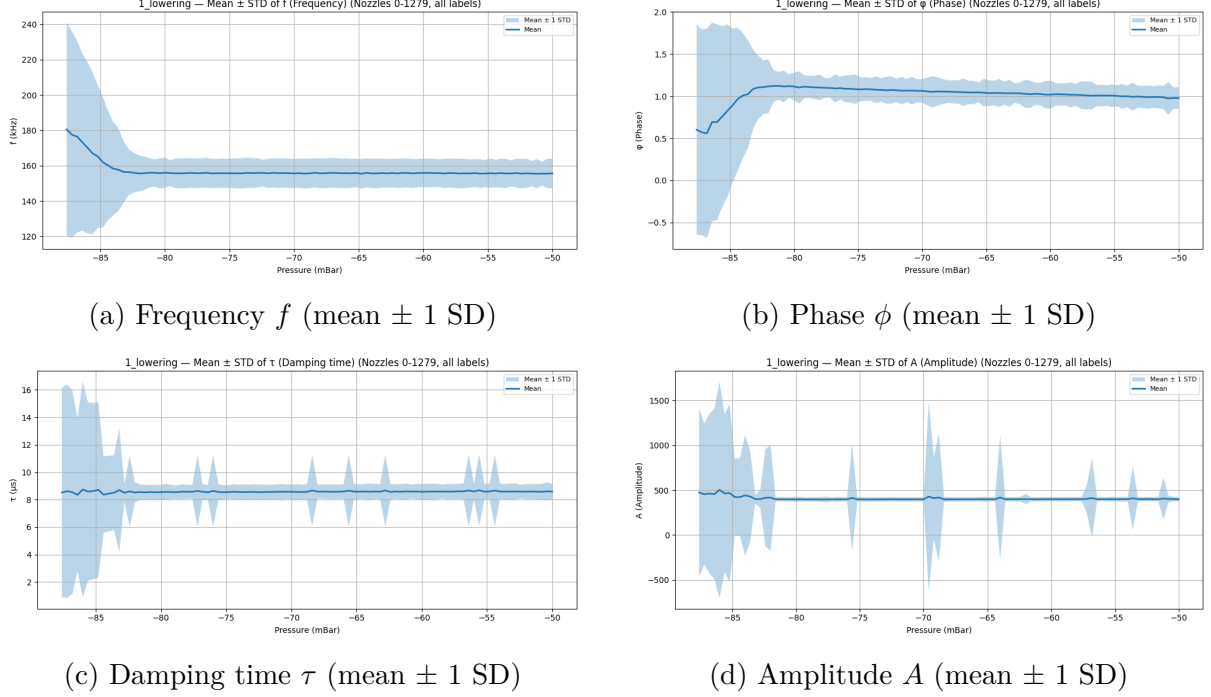(d) Amplitude A (mean $\pm$ 1 SD)

Figure 5.3: Lowering replicate 1: mean $\pm$ standard deviation of fitted ring-down parameters across nozzles as a function of pressure (computed over all labels). Frequency f and phase ϕ exhibit pronounced pressure-dependent drift and increased dispersion in the low-pressure tail, whereas τ and A are comparatively stable over most of the sweep.

5.2 Predictive maintenance results

We evaluate the predictive–maintenance task introduced in Section 4.5 using a *single* histogram–based gradient boosting classifier trained on the first lowering replicate. A nozzle–level split is held fixed throughout, and the training set is constructed by pooling a balanced set of examples extracted at multiple lead times $K \in \{1, \ldots, 10\}$. At evaluation time, performance is reported *separately for each K* by extracting features exactly K steps before the onset index and computing standard classification metrics on four evaluation sets: a balanced held–out subset from the training replicate, the full training replicate excluding training nozzles, and two unseen sequences (lowering replicate 2 and increasing replicate 1).

Horizon dependence. Across datasets, predictive performance is highly concentrated at the shortest horizon. Figure 5.5 shows that the F1 score peaks at $K = 1$ and then drops rapidly as K increases, approaching a low baseline for longer lead times. This behaviour is consistent with a predominantly *abrupt* transition into the non–jetting state: the ring–down parameters contain a detectable precursor immediately before the flip, but provide limited predictive information several steps earlier.

28

Error mode. The confusion matrices in Fig. 5.4 illustrate the associated failure pattern. At $K = 1$, the classifier captures a meaningful fraction of impending flips across lowering replicates and retains reasonable behaviour on the increasing sweep. At $K = 2$, the dominant degradation is a collapse in sensitivity to the positive class ("will flip"), with predictions skewing toward the negative class ("won't flip"). In practice this manifests as an increased rate of false negatives, i.e., missed impending failures, which directly explains the sharp decline in F1 with horizon.

Notes on the increasing sweep. The increasing sequence contains comparatively few labelled steps per nozzle, so larger lead times correspond to sampling very early in the sweep and can become poorly aligned with the offsets represented during training. This mismatch is reflected in Fig. 5.5, where the increasing curve deteriorates more quickly and may degenerate at the largest horizons.

Dataset (lead time K)	Accuracy	Precision	Recall	F1
Lowering rep. 1 (held–out balanced, $K = 1$)	0.876	0.932	0.812	0.868
Lowering rep. 1 (full excl. train, $K = 1$)	0.859	0.775	0.812	0.793
Lowering rep. 2 (full, $K = 1$)	0.872	0.791	0.857	0.823
Increasing rep. 1 (full, $K = 1$)	0.764	0.749	0.882	0.810
Lowering rep. 1 (held–out balanced, $K = 2$)	0.671	0.809	0.447	0.576
Lowering rep. 1 (full excl. train, $K = 2$)	0.745	0.679	0.447	0.539
Lowering rep. 2 (full, $K = 2$)	0.738	0.678	0.467	0.553
Increasing rep. 1 (full, $K = 2$)	0.518	0.686	0.285	0.402

Table 5.2: Predictive–maintenance performance at short horizons. The classifier is trained once on the first lowering replicate using pooled training examples from $K = 1..10$, then evaluated at each lead time K by extracting features K steps before onset. The positive class is *will flip* (impending transition to non–jetting).
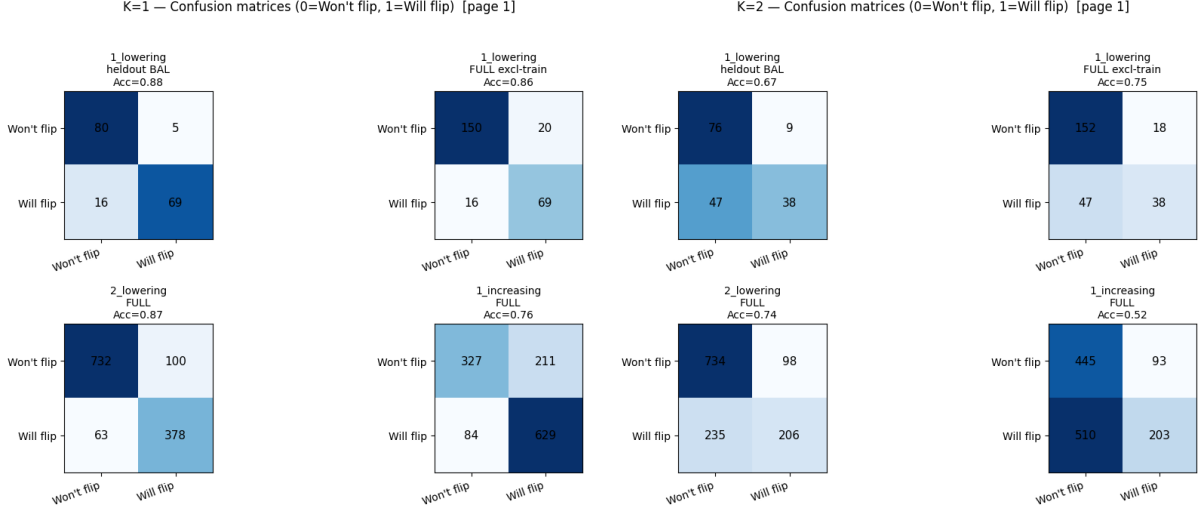
(a) Confusion matrices at $K = 1$ across evaluation sets (0 = won't flip, 1 = will flip).

(b) Confusion matrices at $K = 2$, showing the rapid loss of sensitivity to the positive class.

Figure 5.4: Predictive–maintenance confusion matrices at short horizons. Each panel summarises performance across the four evaluation sets (held–out balanced subset of lowering rep. 1, full lowering rep. 1 excl. train nozzles, lowering rep. 2, and increasing rep. 1).
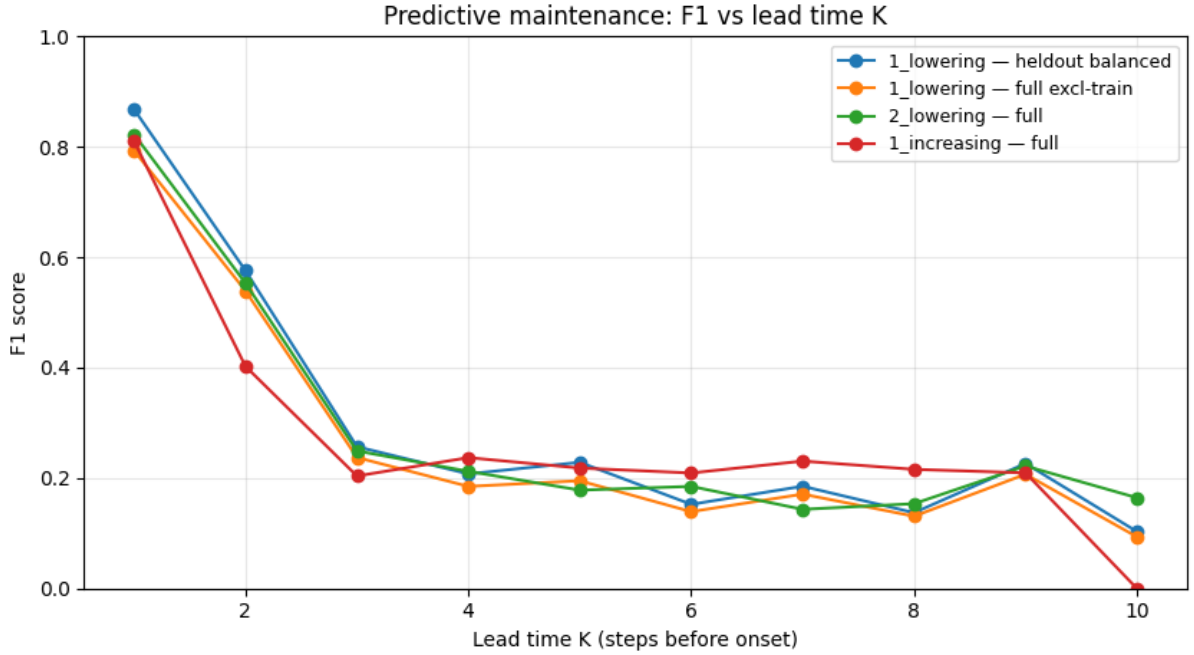

Figure 5.5: Predictive–maintenance performance versus lead time K. A single classifier is trained once on lowering rep. 1 using pooled training examples from $K = 1..10$, then evaluated separately at each K on the four evaluation sets. Curves report the F1 score for the positive class (*will flip*).

Parameter-level illustration (damping time τ). The sharp horizon dependence is also visible directly in the fitted parameters. As an illustrative example, Fig. 5.6 shows the

30

distribution of the damping-time estimate τ stratified by transition groups defined relative to the first non-jetting label. Immediately after onset, τ exhibits a clear distributional shift compared with the early pre-onset regime, whereas the pre-onset window at a fixed offset K becomes progressively less distinguishable from the early regime as K increases. In other words, the class-conditional separation in τ is concentrated in the last few steps before onset and rapidly collapses with lead time due to increasing overlap between the pre-onset and early distributions. This qualitative "regression to baseline" with increasing K is consistent with an abrupt failure transition and explains why predictive performance is dominated by the shortest horizons.

(a) $K = 1$ step before onset. (b) $K = 2$ steps before onset.

(c) $K = 3$ steps before onset. (d) $K = 5$ steps before onset.
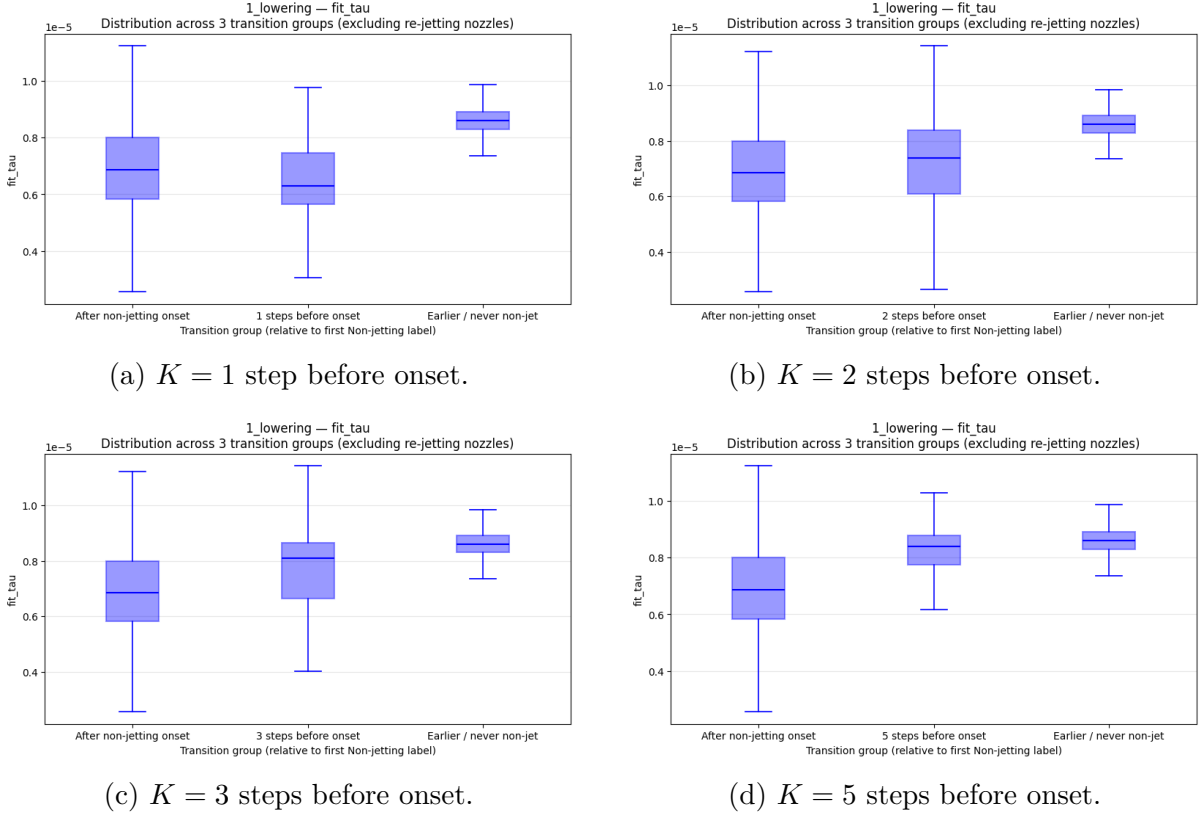
Figure 5.6: Lowering replicate 1: distribution of fitted damping time τ across transition groups defined relative to the first non-jetting label, shown for multiple offsets K (excluding re-jetting nozzles). As K increases, the pre-onset distribution becomes increasingly similar to the early pre-onset regime, indicating that the parameter shift associated with failure is concentrated close to onset and rapidly loses separability at longer lead times.

5.3 Exploratory pressure regression results

We trained a histogram-based gradient boosting regressor to predict the meniscus pressure p from the six fitted ring-down parameters (A, τ, f, ϕ, C, D), using a nozzle-level split (Section 4.6). On held-out nozzles, the model achieves $R^2 \approx 0.51$ with a mean absolute error of about $6\,\mathrm{mbar}$ (RMSE $7.7\,\mathrm{mbar}$).
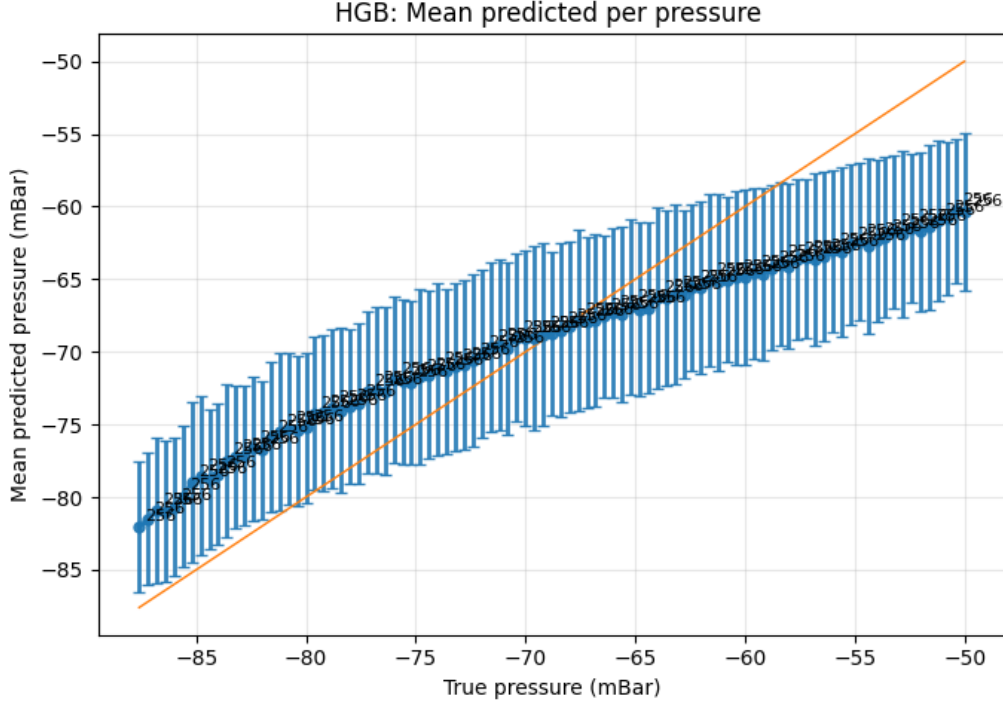
Figure 5.7: Exploratory pressure regression: mean predicted pressure per true pressure level with one standard deviation error bars. Deviations from the diagonal reveal systematic under- and over-estimation near the ends of the pressure range.

Figure 5.7 plots the mean predicted pressure as a function of the true pressure level. Predictions follow the overall trend of the sweep, but the regressor compresses the dynamic range: near the extremes it tends to under-estimate the magnitude, i.e., it predicts pressures closer to the centre of the range than the ground truth. This behaviour is consistent with a strong but imperfect pressure signature in the acoustic parameters, combined with nozzle-to-nozzle variability and measurement noise.

Overall, this experiment confirms that pressure is a major driver of the fitted parameters, but not the only one. This matters for interpretation: strong classification performance can reflect genuine defect signatures, but it can also partially exploit pressure-linked structure in the dataset. This motivates the robustness checks on alternative sweeps and, ultimately, collecting datasets where defects arise under more stable operating conditions.

5.4 Observations on pressure-sweep behaviour

Qualitative inspection of the datasets reveals several patterns that inform later analysis:

- **Defect distribution over pressure.** Missing-line defects are scarce in the mid-range of the pressure sweep but become more frequent at the lowest and highest pressures, consistent with physical expectations of starvation and instabilities.
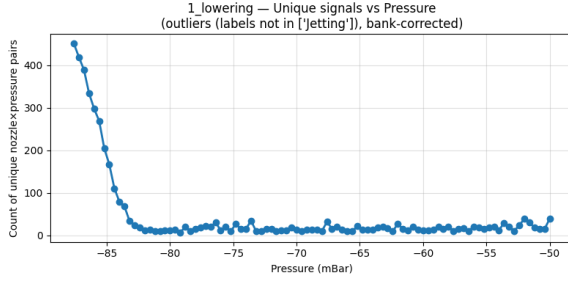
(a) Lowering replicate 1.
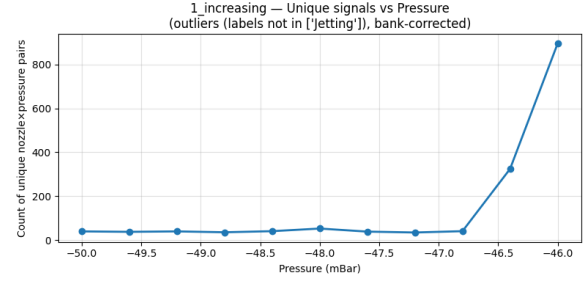
(b) Increasing replicate 1.

Figure 5.8: Defect prevalence versus pressure, quantified as the number of *unique* nozzle×pressure pairs whose label is *not* jetting (i.e., outliers:*n*on-jetting, intermittent or deviated).

- **Spatial clustering across columns.** Defects often manifest in contiguous columns of the printhead: neighbouring nozzles along the cross-web direction fail together, suggesting shared fluidic channels or local wetting patterns. Figure 5.9 shows a representative nozzle-check print where missing lines cluster in columns.
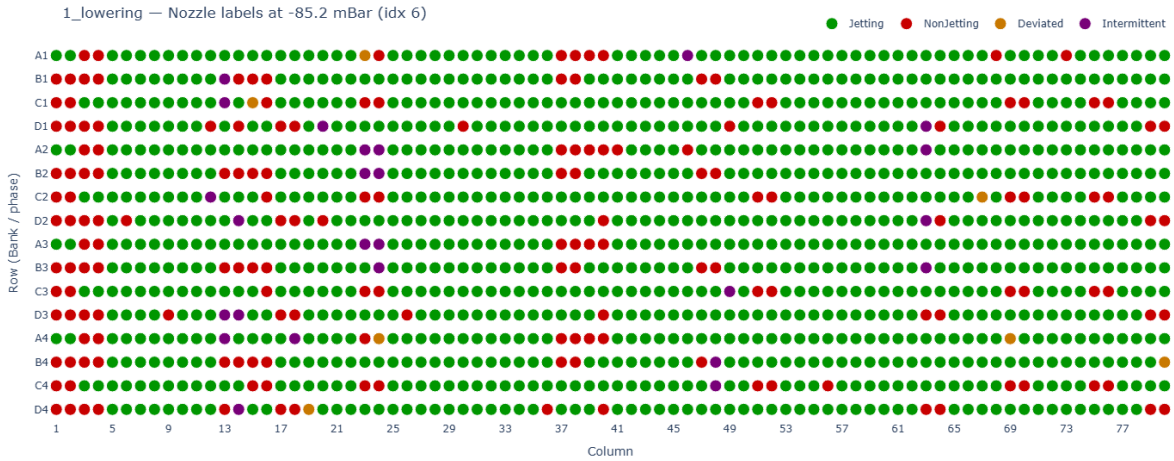
Figure 5.9: Representative nozzle-check map illustrating spatial clustering of defects across columns. Each marker corresponds to a nozzle at a fixed pressure step (here, lowering replicate 1 at $-85.2\,\mathrm{mBar}$), colored by the assigned state (jetting, non-jetting, deviated, intermittent). Non-jetting (red) states appear in contiguous column segments spanning multiple banks/rows, indicating correlated failures along the cross-web direction consistent with shared fluidic channels or local wetting conditions.

These qualitative findings complement the quantitative classification and predictive-maintenance results presented in Chapter 5 and help interpret model behaviour.

5.5 Limitations and outlook

The datasets used here simulate defects by varying pressure rather than by long-term wear and tear. Consequently, missing lines tend to coincide with particular pressure ranges, and it is difficult to disentangle whether the acoustic features predict pressure, defect, or both. The exploratory pressure regression provides a partial diagnosis of this confounding, but more realistic datasets are required to draw definitive conclusions about predictive maintenance. Furthermore, the present work excludes intermittent and deviated labels, which may be relevant in other contexts. Extending the pipeline to multi-class defect taxonomies remains an open avenue.

To address these limitations, future work should:

- Collect datasets where defects arise from natural fouling, clogging or wear, under stable operating conditions.

- Investigate domain adaptation techniques to transfer models across printheads, inks and drive waveforms.

- Explore richer acoustic features (e.g. time-frequency transforms, learned representations) and temporal models that exploit the full pressure-time trajectory.

Chapter 6

Conclusion

This work developed and evaluated an end-to-end pipeline for predictive maintenance of piezoelectric inkjet printheads using acoustic self-sensing. By isolating the informative ring-down segment and fitting a physically interpretable damped-sinusoid model via robust windowed optimisation, we obtained compact six-dimensional feature vectors summarising each nozzle's dynamics. A deterministic bank-correction step enforced a consistent phase convention across banks, enabling direct comparison of fitted parameters across the full printhead.

Nozzle-state inference. Across the lowering sweeps, the histogram-based gradient boosting classifier achieves near-perfect discrimination between jetting and missing-line (non-jetting) states, with errors dominated by conservative false alarms rather than missed defects (Table 5.1 and Fig. 5.1). Importantly, this decision rule transfers to an unseen lowering replicate and remains strong on the increasing-pressure sequence, indicating that the fitted ring-down parameters encode a robust defect signature that generalises across replicates and pressure trajectories.

Predictive maintenance. For anticipatory forecasting, performance is strongly horizon-dependent: the usable early-warning signal is concentrated at the shortest lead time and degrades rapidly as the horizon increases (Fig. 5.5). This behaviour is consistent with a predominantly abrupt transition into the non-jetting state, where the fitted parameters exhibit a detectable change only shortly before onset. Consistent with this, the τ boxplots show that the pre-onset shift is concentrated near onset and rapidly vanishes as the lead time increases (Fig. 5.6).

Qualitative structure and confounding. Beyond aggregate metrics, defects exhibit systematic structure: they concentrate toward pressure-range extremes and

often cluster in contiguous printhead columns, suggesting correlated failures along shared fluidic paths or local wetting conditions (Fig. 5.8 and Fig. 5.9). Finally, although pressure is not provided as an input to the classifiers, exploratory analyses confirm that pressure explains a substantial fraction of the acoustic variability, underscoring that pressure-controlled defect simulation can act as a confounder and must be considered when interpreting generalisation to real production data (Section 5.3).

Outlook. The next step toward deployment is to validate the approach on datasets where defects arise naturally under stable operating conditions (fouling, clogging, wear), reducing pressure-induced confounding. Promising extensions include incorporating spatial context explicitly (column-aware features or structured models), learning richer acoustic representations to improve robustness under domain shifts, and extending the current binary labels to cover intermittent and deviated states.

Bibliography

[1] T. H. Phung, S. H. Park, I. Kim, T.-M. Lee, and K.-S. Kwon, "Machine learning approach to monitor inkjet jetting status based on the piezo self-sensing," *Scientific Reports*, vol. 13, no. 1, p. 18089, Oct. 2023, publisher: Nature Publishing Group. [Online]. Available: https://www.nature.com/articles/s41598-023-45445-0

[2] K.-S. Kwon and J. Y. Jo, "Towards zero-defect inkjet printing via piezo self-sensing signals," *Sensors and Actuators A: Physical*, vol. 393, p. 116755, Oct. 2025. [Online]. Available: https://www.sciencedirect.com/science/article/pii/S0924424725005618

[3] L. Bullot, C. C. Ull, S. Filliger, and L. Brügger, "Piezoelectric-based Monitoring of Pressure Variations in Inkjet Printhead," *Advanced Inkjet Technology*, vol. 1, no. 1, pp. 21–24, Jan. 2024. [Online]. Available: https://library.imaging.org/AdvInkjetTech/articles/1/1/5

[4] P. Malhotra, A. Ramakrishnan, G. Anand, L. Vig, P. Agarwal, and G. Shroff, "LSTM-based Encoder-Decoder for Multi-sensor Anomaly Detection," Jul. 2016, arXiv:1607.00148 [cs]. [Online]. Available: http://arxiv.org/abs/1607.00148

[5] Y. Su, Y. Zhao, C. Niu, R. Liu, W. Sun, and D. Pei, "Robust Anomaly Detection for Multivariate Time Series through Stochastic Recurrent Neural Network," in *Proceedings of the 25th ACM SIGKDD International Conference on Knowledge Discovery & Data Mining.* Anchorage AK USA: ACM, Jul. 2019, pp. 2828–2837. [Online]. Available: https://dl.acm.org/doi/10.1145/3292500.3330672

[6] S. Kilickaya, M. Ahishali, C. Celebioglu, F. Sohrab, L. Eren, T. Ince, M. Askar, and M. Gabbouj, "Audio-based Anomaly Detection in Industrial Machines Using Deep One-Class Support Vector Data Description," in *2025 IEEE Symposium on Computational Intelligence on Engineering/Cyber Physical Systems Companion (CIES Companion)*, Mar. 2025, pp. 1–5, arXiv:2412.10792 [cs]. [Online]. Available: http://arxiv.org/abs/2412.10792

[7] J. Audibert, P. Michiardi, F. Guyard, S. Marti, and M. A. Zuluaga, "USAD: UnSupervised Anomaly Detection on Multivariate Time Series," in *Proceedings of the 26th ACM SIGKDD International Conference on Knowledge Discovery & Data Mining.* Virtual Event CA USA: ACM, Aug. 2020, pp. 3395–3404. [Online]. Available: https://dl.acm.org/doi/10.1145/3394486.3403392

[8] V. Chandola, A. Banerjee, and V. Kumar, "Anomaly detection: A survey," *ACM Comput. Surv.*, vol. 41, no. 3, pp. 15:1–15:58, Jul. 2009. [Online]. Available: https://doi.org/10.1145/1541880.1541882

[9] M. A. Pimentel, D. A. Clifton, L. Clifton, and L. Tarassenko, "A review of novelty detection," *Signal Processing*, vol. 99, pp. 215–249, Jun. 2014. [Online]. Available: https://linkinghub.elsevier.com/retrieve/pii/S016516841300515X

Appendix A

Additional parameter diagnostics

This appendix provides additional diagnostic plots for the fitted ring-down parameters on lowering replicate 1. For each quantity, we show (left) the mean ± standard deviation across nozzles as a function of pressure (computed over all labels), and (right) the distribution of the fitted parameter stratified by ISIS nozzle-state labels. For the boxplots (right panels), the central line denotes the median, while the lower and upper edges of the box correspond to the 25th and 75th percentiles (interquartile range), shown separately for each ISIS nozzle-state label.
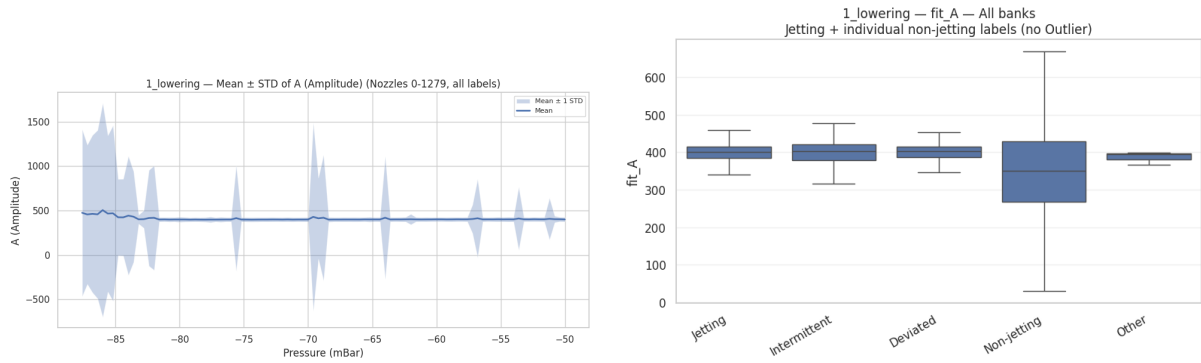
(a) Mean ± SD of amplitude A versus pressure.

(b) Amplitude A by label.

Figure A.1: Amplitude diagnostics on lowering replicate 1.
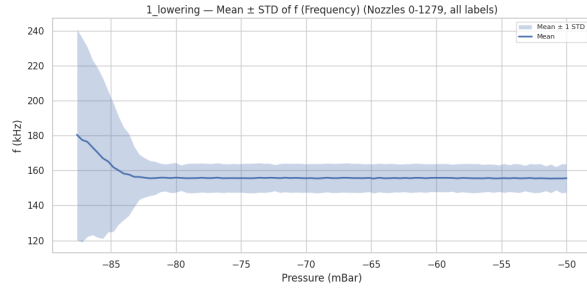
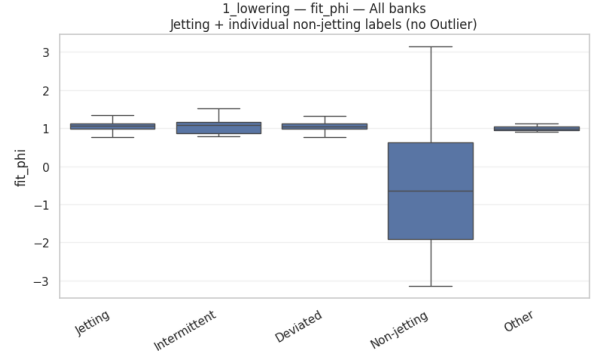(a) Mean $\pm$ SD of frequency f versus pressure.
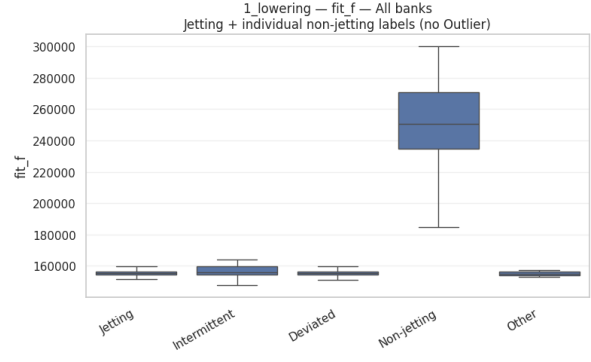
(b) Frequency f by label.

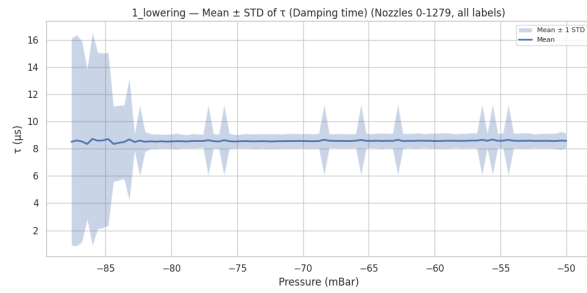Figure A.2: Frequency diagnostics on lowering replicate 1.
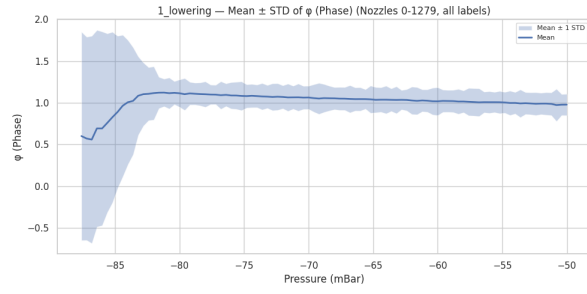
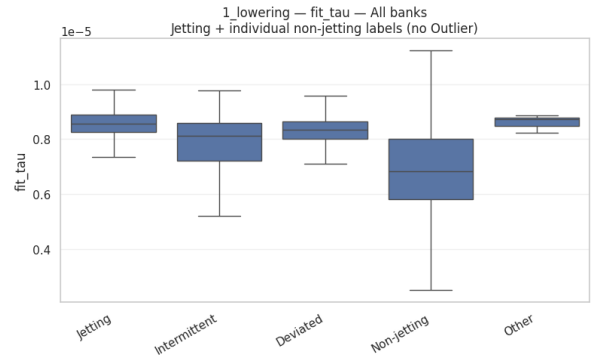(a) Mean $\pm$ SD of phase ϕ versus pressure.

(b) Phase ϕ by label.

Figure A.3: Phase diagnostics on lowering replicate 1.
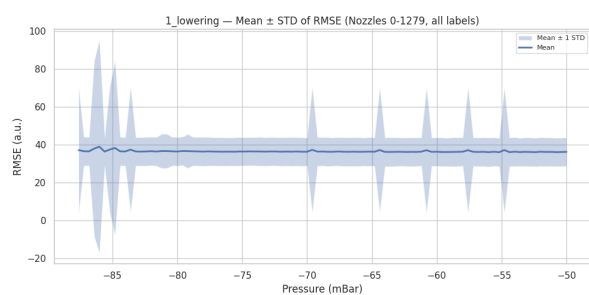

(a) Mean $\pm$ SD of damping time τ versus pressure.
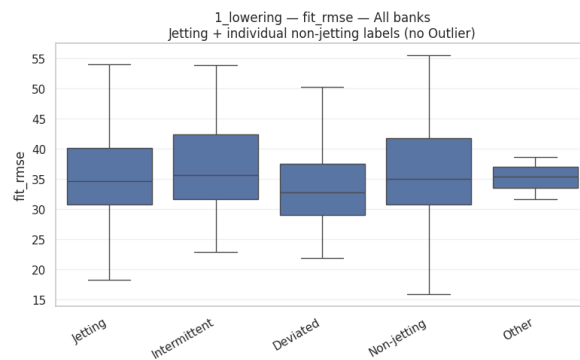

(b) Damping time τ by label.

Figure A.4: Damping-time diagnostics on lowering replicate 1.

(a) Mean ± SD of RMSE versus pressure.

(b) RMSE by label.

Figure A.5: Fit-error diagnostics (RMSE) on lowering replicate 1.